Co, Mn co-doped Fe_9S_{11}@Ni_9S_8 supported on nickel foam as high efficiency electrocatalyst for oxygen evolution reaction and urea oxidation reaction

Jiaxin Li[a], Lixin Zhang[a], Xiaoqiang Du[a*] and Xiaoshuang Zhang[b]

[a] Shanxi Key Laboratory of High Performance Battery Materials and Devices, School of Chemical Engineering and Technology, North University of China, Xueyuan road 3, Taiyuan 030051, People's Republic of China. E-mail: duxq16@nuc.edu.cn

[b] School of Science, North University of China, Xueyuan road 3, Taiyuan 030051, People's Republic of China.

Preparation of IrO_2@NF

20 mg of IrO_2 was added to 1 mL of mixed solution of ethanol solution and Nafion solution with the ratio of 19 : 1, then the above mixture was sonicated for 30 minutes to ensure the formation of a homogeneous suspension. Subsequently, 200 μL of solution was evenly dropped on bare NF (1 cm^2 in area), and dried at room temperature.

DFT calculation

The DFT calculations were performed using the Cambridge Sequential Total Energy Package (CASTEP) with the plane-wave pseudo-potential method. The geometrical structures of the (003) plane of Fe-NiOOH, Co-Fe-NiOOH and Mn-Co-Fe-NiOOH were optimized by the generalized gradient approximation (GGA) methods. The Revised Perdew-Burke-Ernzerh of (RPBE) functional was used to treat the electron exchange correlation interactions. A Monkhorst Pack grid k-points of 7*7*1 of Fe-NiOOH, Co-Fe-NiOOH and Mn-Co-Fe-NiOOH, a plane-wave basis set cut-off energy of 480 eV were used for integration of the Brillouin zone. The structures were optimized for energy and force convergence set at 0.05 eV/A and 2.0×10^{-5} eV, respectively. The vacuum space was up to 0.002 A to eliminate periodic interactions.

Gas detection. The same volume of gas sample in the headspace of the electrolytic cell was withdrawn by a SGE gas-tight syringe and analyzed by gas chromatography (GC). The O_2 in the sampled gas was separated by passing through a 2 m × 3 mm packed molecular sieve 5A column with an Ar carrier gas and quantified by a Thermal Conductivity Detector (TCD) (Shimadzu GC-9A).(Res: Dalton Trans., 2022, 51, 2444-2451)

Turnover frequency (TOF) calculations: To calculate TOF, we need to calculate the surface

concentration of active sites associated with the redox Co, Mn, Fe and Ni species by electrochemistry. The linear relationship between the plot of the oxidation peak current densities for redox Co, Mn, Fe and Ni species and scan rates can be derived from the electrochemical cyclic voltammetry scans according to the following equation:

Slope = $n^2F^2A\,\Gamma_0/RT$

Where n representing the number of electrons transferred is 1 assuming a one–electron process for oxidation of Co, Mn, Fe and Ni centers in Co-Mn-Fe_9S_{11}@Ni_9S_8; F is Faraday's constant (96485 C mol^{-1}); A is the geometrical surface area of the electrode; Γ_0 is the surface concentration of active sites (mol cm^{-2}), and R and T are the ideal gas constant and the absolute temperature, respectively.

TOF values can be finally calculated based on the formula:

TOF = $jA/4Fm$

Where j is the current density, 4 indicate the mole of electrons consumed for one mole of O_2 evolution, and m is the mole number of active sites. (Res: Dalton Trans., 2022, 51, 2444-2451)

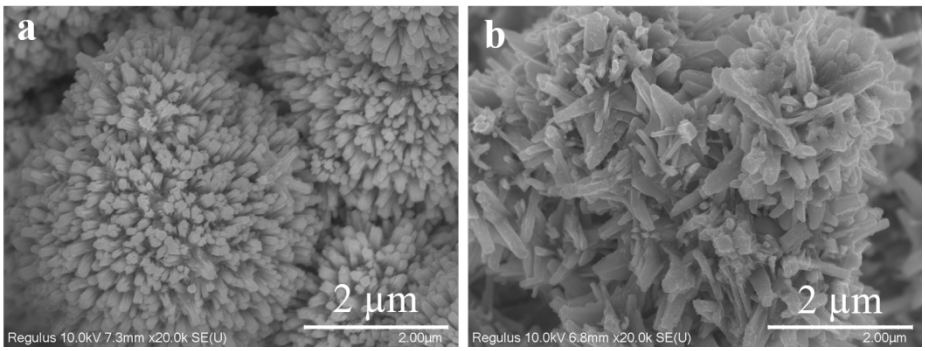

Fig. S1. SEM images of Co-Fe_9S_{11}@Ni_9S_8/NF(a) and Mn-Fe_9S_{11}@Ni_9S_8/NF(b).

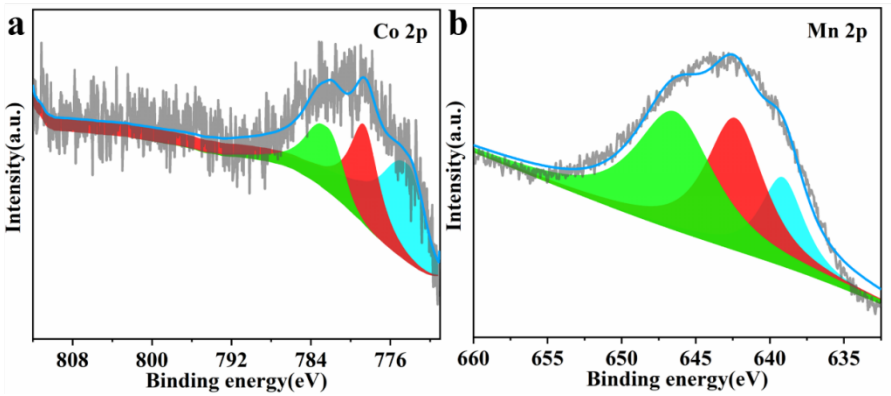

Fig. S2. XPS spectra of (a) Co 2p; (b) Mn 2p for Co-Mn-Fe_9S_{11}@Ni_9S_8/NF.

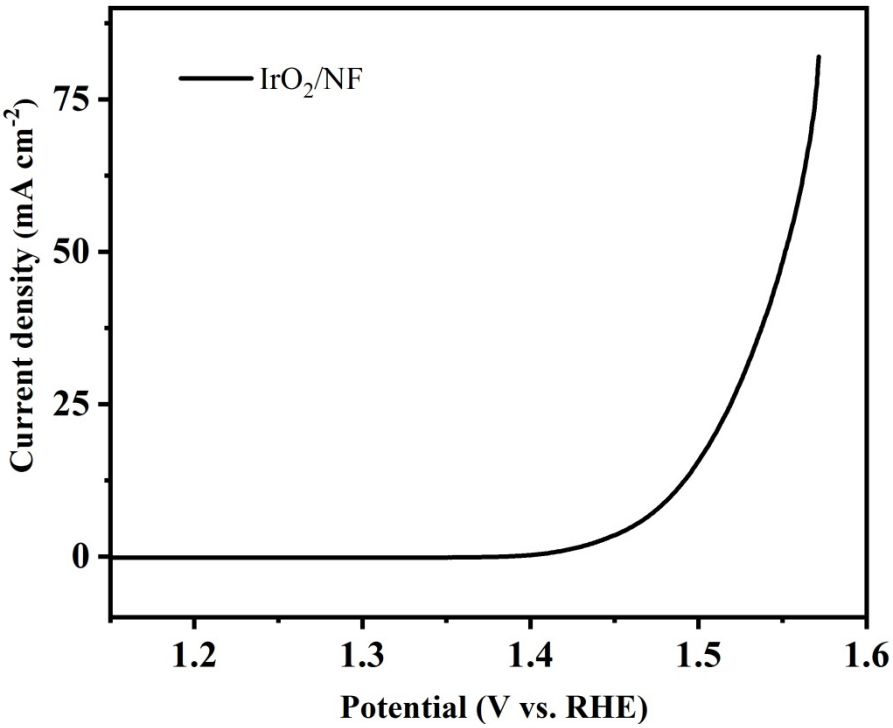

Fig. S3. Polarization curve of the IrO_2 for OER with a scan rate of 5 mV s^{-1} in 1 M KOH.

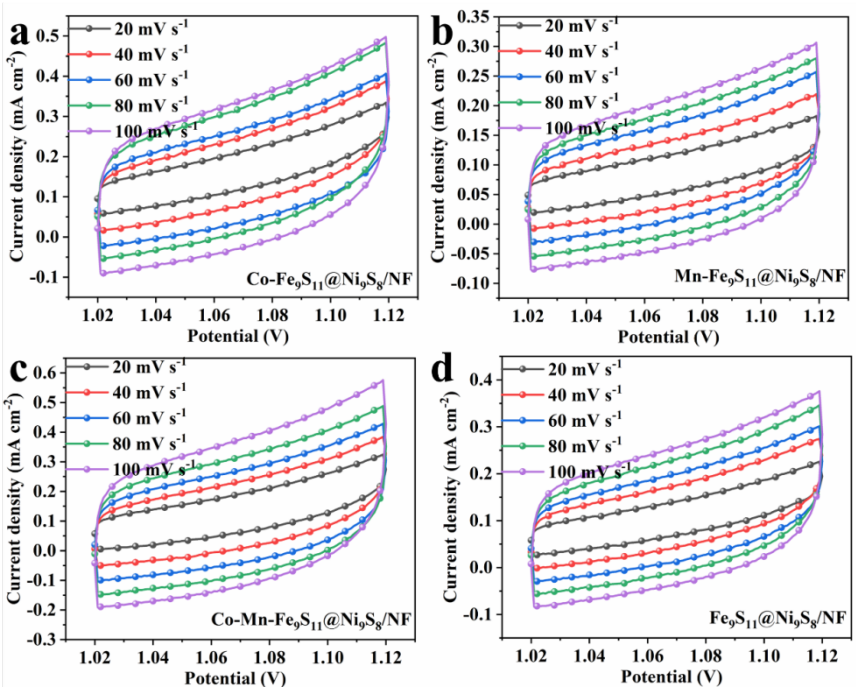

Fig. S4. CV curves of Co-Fe_9S_{11}@Ni_9S_8/NF(a), Mn-Fe_9S_{11}@Ni_9S_8/NF(b), Co-Mn-Fe_9S_{11}@Ni_9S_8/NF(c) and Fe_9S_{11}@Ni_9S_8/NF(d) for OER.

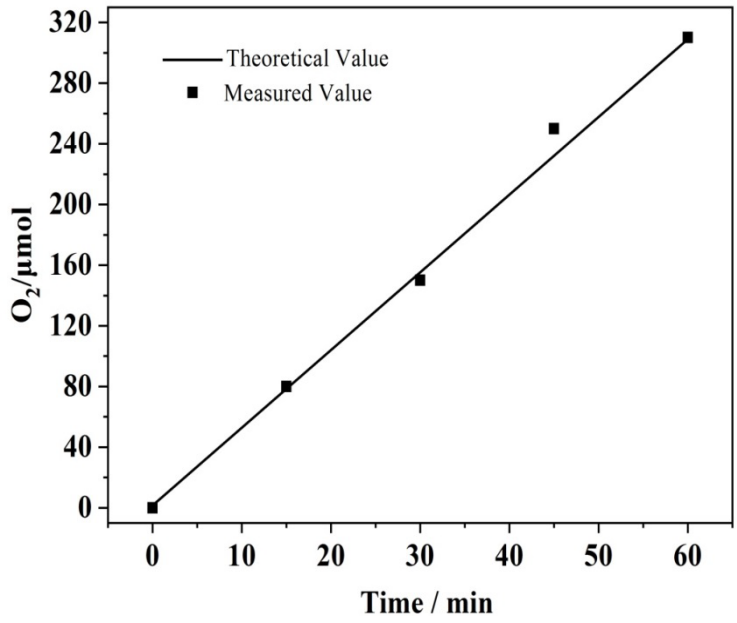

Fig. S5. Electrocatalytic efficiency of O_2 production over Co-Mn-Fe_9S_{11}@Ni_9S_8/NF.

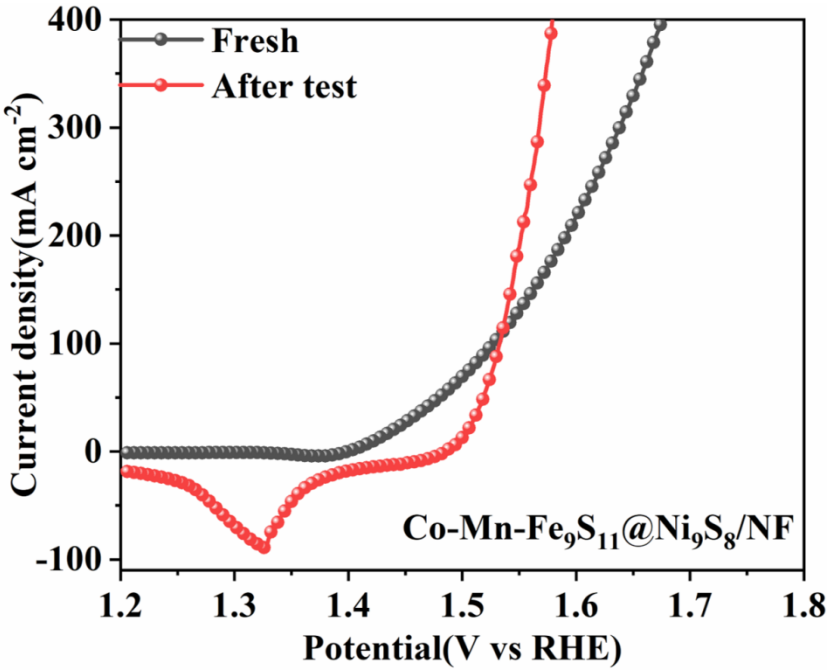

Fig. S6. LSV curves of Co-Mn-Fe_9S_{11}@Ni_9S_8/NF fresh and after OER test.

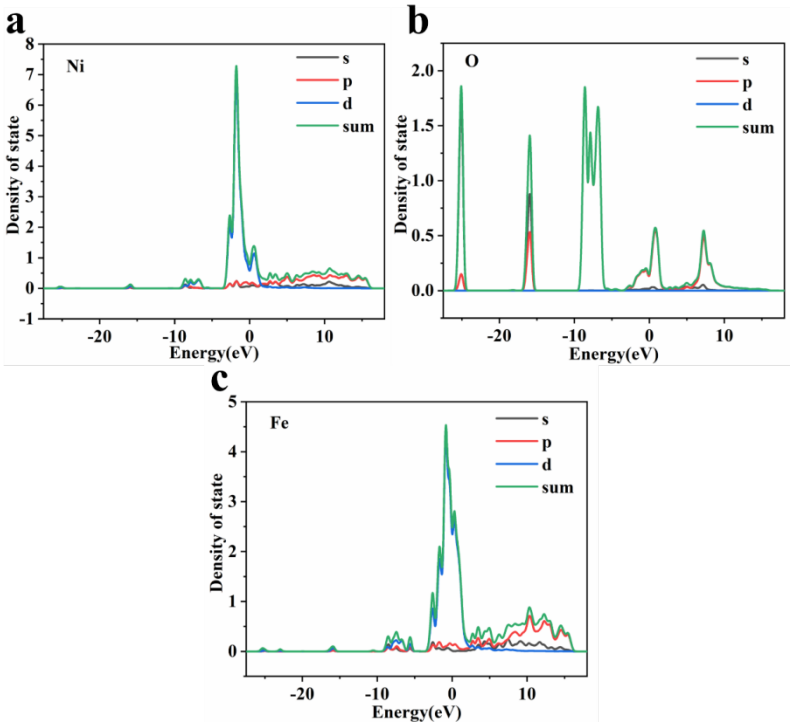

Fig. S7. Density of states for Fe-NiOOH, (a) Ni, (b) O and (c)Fe.

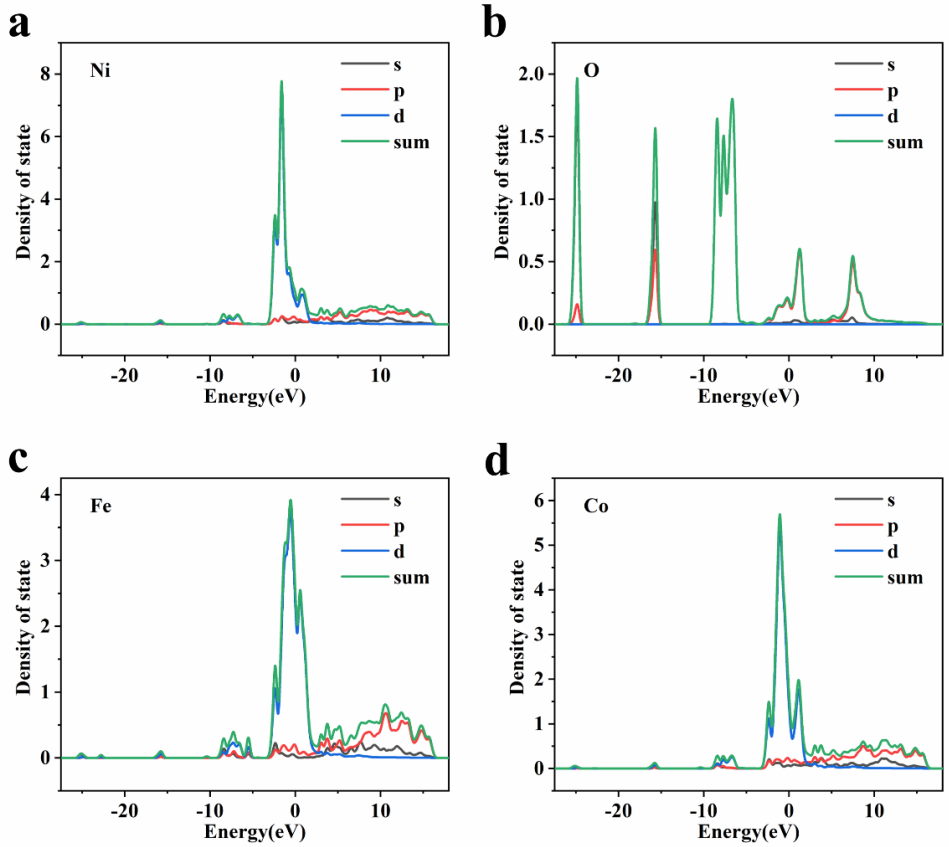

Fig. S8. Density of states for Co-Fe-NiOOH, (a) Ni, (b) O, (c)Fe and (d)Co.

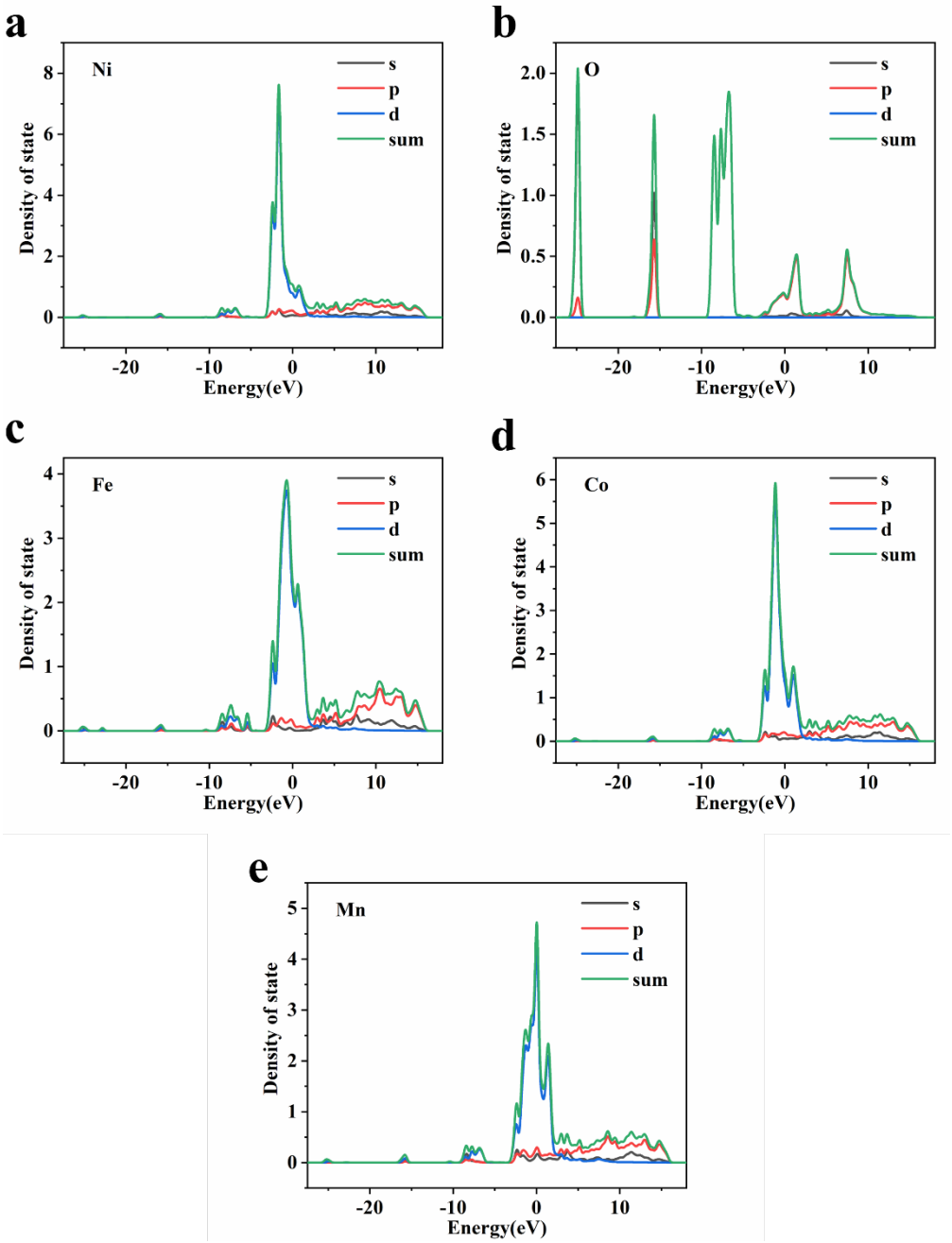

Fig. S9. Density of states for Mn-Co-Fe-NiOOH, (a) Ni, (b) O, (c)Fe, (d)Co and (e)Mn.

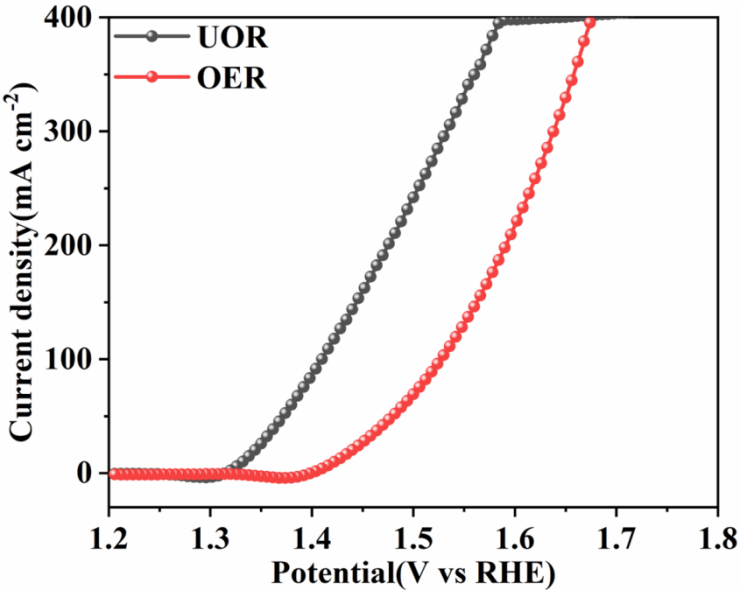

Fig. S10. Polarization curves of OER and UOR for Co-Mn-Fe_9S_{11}@Ni_9S_8/NF.

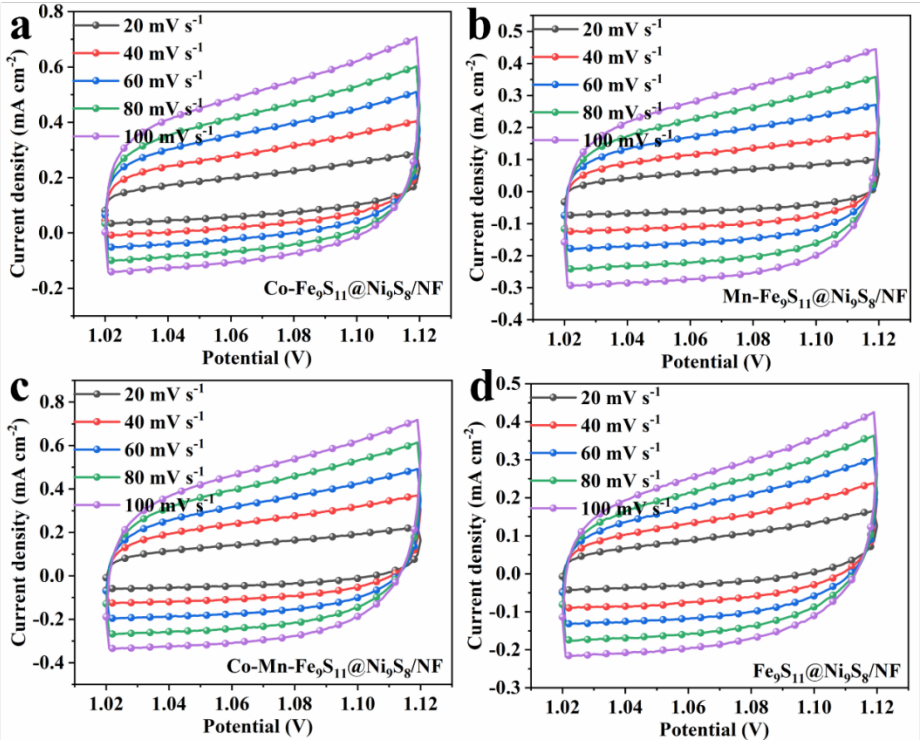

Fig. S11.CV curves of Co-Fe_9S_{11}@Ni_9S_8/NF(a), Mn-Fe_9S_{11}@Ni_9S_8/NF(b), Co-Mn-Fe_9S_{11}@Ni_9S_8/NF(c) and Fe_9S_{11}@Ni_9S_8/NF for UOR(d).

Table S1. Comparison of OER performances of reported electrocatalyst in 1.0 M KOH

Materials	η@10 mA cm^{-2} (mV)	η@20 mA cm^{-2} (mV)	Ref.
Ni/MoO_2@CN	250	262	[1]
$NiSe_2/Ni_3Se_4$/NF-1	234	260	[2]
$Co/Mo_2C/Co_6Mo_6C_2$@C/750SA	281	300	[3]
Mn-NiO-400	265	287	[4]
CoNiFe–Se@C	273	307	[5]
$CoNiFe_2O_5 \cdot 2CuO$	264	286	[6]
FeS_2-MoS_2@CoS_2-MOF	194	211	[7]
N-Fe-Ni_3S_2@NiP_2/NF	-	251@100 mA cm^{-2}	[8]
Co-Mn-Fe_9S_{11}@Ni_9S_8/NF	**193**	**210**	**This work**

Table S2. Comparison of UOR performances of reported electrocatalyst in 1.0 M KOH

Materials	η@10 mA cm^{-2} (V)	η@20 mA cm^{-2} (V)	Ref.
NiFeCoSx@$FeNi_3$	1.42	-	[9]
Fc-MOF	1.35	-	[10]
CoFe LDH/MOF-0.06	1.45	-	[11]
NiF_3/Ni_2P@CC-2	1.36	-	[12]
$Ni_9S_8/CuS/Cu_2O$/NF	1.357	-	[13]
U-NiMn-LDH/CFC	-	1.351	[14]
NiMo@ZnO/NF	1.405	-	[15]
N-Fe-Ni_3S_2@NiP_2/NF	1.353@100 mA cm^{-2}		[8]
Co-Mn-Fe_9S_{11}@Ni_9S_8/NF	**1.33**	**1.34**	**This work**

[1] G. Qian, J. Chen, T. Yu, J. Liu, L. Luo, S. Yin, Three-Phase Heterojunction NiMo-Based

Nano-Needle for Water Splitting at Industrial Alkaline Condition;Nano-Micro Lett., 2022;14: 20.

[2] L. Tan, J. Yu, H. Wang, H. Gao, X. Liu, L. Wang, X. She, T. Zhan, Controllable synthesis and phase-dependent catalytic performance of dual-phase nickel selenides on Ni foam for overall water splitting;Appl. Catal., B, 2022;303: 120915.

[3] W. Yaseen, M. Xie, B.A. Yusuf, Y. Xu, N. Ullah, M. Rafiq, A. Ali, J. Xie, Synergistically coupling of Co/Mo2C/Co6Mo6C2@C electrocatalyst for overall water splitting: The role of carbon precursors in structural engineering and catalytic activity;Appl. Surf. Sci., 2022;579: 152148.

[4] Y. Liu, L. Bai, T. Li, J. Huo, X. Wang, L. Zhang, X. Hao, S. Guo, Mn-doping tuned electron configuration and oxygen vacancies in NiO nanoparticles for stable electrocatalytic oxygen evolution reaction;Appl. Surf. Sci., 2022;577: 151952.

[5] A. El Jaouhari, A. Slassi, B. Zhang, W. Liu, D. Cornil, J. Zhu, X. Wu, D. Zhou, X. Liu, Enhancement of oxygen evolution reaction by X-doped (X 1/4 Se, S, P) holey graphitic carbon shell encapsulating NiCoFe nanoparticles: a combined experimental and theoretical study;Mater. Today Chem., 2022;23: 100706.

[6] P. Wang, R. Zhao, F. Zhang, J. Wang, B. Han, Z. Liu, Interface engineered Co, Ni, Fe, Cu oxide hybrids with biphasic structures for water splitting with enhanced activity;J. Colloid Interface Sci., 1800;609: 149-57.

[7] K. Chhetri, A. Muthurasu, B. Dahal, T. Kim, T. Mukhiya, S.h. Chae, T.H. Ko, Y.C. Choi, H.Y. Kim, Engineering the abundant heterointerfaces of integrated bimetallic sulfide-coupled 2D MOF-derived mesoporous CoS2 nanoarray hybrids for electrocatalytic water splitting;Mater. Today Nano, 2022;17: 100146.

[8] J. Li, H. Cui, X. Du, X. Zhang, The controlled synthesis of nitrogen and iron co-doped Ni3S2@NiP2 heterostructures for the oxygen evolution reaction and urea oxidation reaction;Dalton Trans., 2022;51: 2444-51.

[9] J. Shen, Q. Li, W. Zhang, Z. Cai, L. Cui, X. Liu, J. Liu, Spherical Co3S4 grown directly on Ni-Fe sulfides as a porous nanoplate array on FeNi3 foam: a highly efficient and durable bifunctional catalyst for overall water splitting;J. Mater. Chem. A, 2022;10: 5442-51.

[10] M. Li, H. Sun, J. Yang, M. Humayun, L. Li, X. Xu, X. Xue, A. Habibi-Yangjeh, K. Temst, C. Wang, Mono-coordinated metallocene ligands endow metal-organic frameworks with highly efficient oxygen evolution and urea electrolysis;Chem. Eng. J., 2022;430: 132733.

[11] S. Huang, Y. Wu, J. Fu, P. Xin, Q. Zhang, Z. Jin, J. Zhang, Z. Hu, Z. Chen, Hierarchical CoFe LDH/MOF nanorods array with strong coupling effect grown on carbon cloth enables efficient oxidation of water and urea;Nanotechnol., 2021;32: 385405.

[12] K. Wang, W. Huang, Q. Cao, Y. Zhao, X. Sun, R. Ding, W. Lin, E. Liu, P. Gao, Engineering NiF3/Ni2P heterojunction as efficient electrocatalysts for urea oxidation and splitting;Chem. Eng. J., 2022;427: 130865.

[13] D. Wei, W. Tang, Y. Wang, Hairy sphere-like Ni9S8/CuS/Cu2O composites grown on nickel foam as bifunctional electrocatalysts for hydrogen evolution and urea electrooxidation;Int. J. Hydrogen Energy, 2021;46: 20950-60.

[14] G. Liu, C. Huang, Z. Yang, J. Su, W. Zhang, Ultrathin NiMn-LDH nanosheet structured electrocatalyst for enhanced electrocatalytic urea oxidation;Appl. Catal., A, 2021;614: 118049.

[15] J. Cao, H. Li, R. Zhu, L. Ma, K. Zhou, Q. Wei, F. Luo, Improved hydrogen generation via a urea-assisted method over 3D hierarchical NiMo-based composite microrod arrays;J. Alloys Compd., 2020;844: 155382.